Supporting Information

Simon Cabanes*[1], Stefania Espa[1], Boris Galperin[2], Roland M. B. Young[3], and Peter L. Read[4]

[1]DICEA, Sapienza Universitá di Roma, Via Eudossiana 18, 00184 Rome, Italy.
[2]College of Marine Science, University of South Florida, St. Petersburg, Florida 33701, USA
[3]Department of Physics & National Space Science and Technology Center, UAE University, Al Ain, United Arab Emirates
[4]Atmospheric, Oceanic and Planetary Physics, Department of Physics, University of Oxford, Oxford OX1 3PU, UK.

July 29, 2020

Contents

1 Methods

1.1 Experimental device

Our device is based on several previous set-ups detailed in Espa et al. (2014) and Galperin et al. (2014a, 2016). It consists of a $L_x = 0.68$ by $L_y = 0.69$ m rectangular tank of 0.20 m height that is attached to a rotating table by a rigid aluminium super-structure. The tank is filled with an electrolytic saline solution (mean depth of 4 cm) rotating counterclockwise with angular velocity $\Omega = 3$ rad s^{-1}. A transparent lid insulates the working fluid from the ambient air (The experimental facility is shown in supplementary Fig. 1). The radius of the working section is $R = 0.297$ m and the topographic β-effect $\beta = (2\Omega/H)dH/dr$ is related to the column fluid height,

$$H = H_o + \frac{\Omega^2}{2g}\left(r^2 - \frac{L_x^2 + L_y^2}{12}\right) \tag{1}$$

where r is the cylindrical radius and g is the gravitational constant. In our spectral analysis, β corresponds to the averaged value $\beta = 0.53$ cm^{-1} s^{-1}. The forcing is produced by passing a constant electric current through the working fluid over an array of permanent magnets (12 mm in diameter and spaced by 1-2 cm from each other) mounted under the bottom of the tank in a 90° or 180° arc of a 17 cm radius. Using the magnets' polarity, we can induce a westward and an eastward momentum that drives the formation of westward and eastward zonal

*cabanes.simon@gmail.com

jets. Experiments are run in both configurations for an electrical current intensity that varies between $I = 2, 4$ and 6A, as summarizesd in supplementary Table 1.

Velocities were measured at the flow surface by analyzing images of passively advected styrene particles with a mean size of about 5×10^{-5} m monitored by a video camera with a spatial resolution of 1023×1240 pixels at a frequency of 20 Hz. The acquired images were analyzed using a feature tracking algorithm that reconstructs instantaneous Lagrangian velocities (Lacorata and Espa, 2012). The time history of the Eulerian velocity field was then obtained by interpolating the sparse data over a regular grid. Velocity fields are then projected onto a polar coordinate grid that is more appropriate to derive the spectral decomposition of the flow.

1.2 Spectral analysis in the cylindrical geometry of the laboratory

To compute the spectral analysis of 2D velocity fields $\mathbf{u}$ projected on a polar coordinate grid, we use the truncated Bessel-Fourier decomposition over 90° and 180° sectors (corresponding to the electromagnetic forcing), truncation indices $\gamma = 4$ and 2, respectively:

$$f(r,\varphi) = \sum_{m=-M}^{M} \sum_{n=1}^{N} C_m^n J_m \left(\alpha_{mn} \frac{r}{R}\right) e^{\gamma i m \varphi} \tag{2}$$

where $f(r,\varphi)$ is an arbitrary well-behaving function in cylindrical coordinates (of radius r and azimuth angle φ) such that $f(R,\varphi) = 0$, J_m is the Bessel function of the mth order, α_{mn} its nth zero, n and m are respectively radial and zonal modes, and C_m^n are complex Bessel-Fourier coefficients (Arfken and Weber, 1999). With a spatial resolution of 1°, the total number of zonal modes M is limited to 45 for a 90° sector, 90 for a 180° sector, and the total number of radial modes N are limited to 60. It is clear from Eq. (2) that the 2D kinetic energy spectrum for each pair of modes m and n is

$$E(n,m) = \frac{1}{2} C_m^n \overline{C_m^n} J_{m+1}(\alpha_{mn})^2, \tag{3}$$

with $\overline{C_m^n}$ the complex conjugate of C_m^n. Here the total kinetic energy $E(n,m)$ is the sum of the radial and zonal kinetic energy spectra computed from radial u_r and zonal u_φ velocity components with $\mathbf{u} = u_r \mathbf{e_r} + u_\varphi \mathbf{e}_\varphi$. To accommodate the spectral anisotropy due to a β-effect, we define respectively the zonal and Kolmogorov-Kraichnan (KK) spectra as the axisymmetric part of the energy $E_Z(n) = E(n, m = 0)$ and its non-axisymmetric part $E_{KK}(n) = \sum_{m=-M}^{M} E(n, m \neq 0)$ (Sukoriansky et al., 2002). In cylindrical geometry, When the flow approaches the regime of zonostrophic turbulence (Galperin et al., 2010), the spectra are expected to become

$$E_Z(\alpha_{0n}) \simeq C_Z \beta^2 (\alpha_{0n}/R)^{-5} R^{-1}, \tag{4a}$$

$$E_{KK}(\alpha_{mn}) \simeq C_K \Pi_\epsilon^{2/3} (\alpha_{1n}/R)^{-5/3} R^{-1}, \tag{4b}$$

with constants $C_Z = 0.2$ and $C_K = 6$, and R the tank's radius. One can estimate the scale at which the zonal and KK spectra intersect,

$$\hat{L}_\beta \simeq (C_K/C_Z)^{3/10} (\alpha_{0n}/n)(\alpha_{0n}/\alpha_{1n})^{1/2} (\Pi_\epsilon/\beta^3)^{1/5}. \tag{5}$$

Supplementary Table 1 gives the values of n and $\hat{L}_\beta$ at which the spectra intersect in all experiments. The relationship between $\hat{L}_\beta$ and L_β expressed by Eq. (5) is specific to the polar coordinate system due to the mapping of the space of n onto the space of α_{mn}. In cylindrical geometry, scale $\hat{L}_\beta$ is used for the ratio L_β/L_M reported in the main manuscript Table.

1.3 Kinetic energy flux in the laboratory

In order to better characterize the non-linear dynamics of eddy-eddy interactions, we compute the non-linear energy flux, which provides another estimate of the energy transfer rate, Π_ϵ. Energy flux is obtained in our laboratory experiment by using a filtering procedure applied on a Cartesian 2D velocity field $\mathbf{u}(\mathbf{x})$ as introduced by Chen et al. (2006); Boffetta and Musacchio (2010).

Following their approach, we introduce the filtered velocity field $\mathbf{u}_s(\mathbf{x}) = (G_s * \mathbf{u})(\mathbf{x})$ that contains the information from $\mathbf{u}(\mathbf{x})$ only at length scales $> s$ and results from convolution with a Gaussian filter $G_s(\mathbf{x}) = s^{-2}G(\mathbf{x}/s)$. The energy flux Π_ϵ that represents the local transfer of kinetic energy from scales larger than s to scales smaller to s, is defined as,

$$\Pi_\epsilon^s(\mathbf{x}) = -(\tau_{ij})_s \nabla_i (u_j)_s, \tag{6}$$

where $(\tau_{ij})_s = (u_i u_j)_s - (u_i)_s (u_j)_s$ and ∇_i is the first derivative. Computed from expression (6), fluxes with a negative/positive value evidence an upscale/downscale (inverse/direct) cascade of energy. Figure 1 in the main text and Figure 2 in the Supporting Information show energy fluxes computed on a $N_x \times N_y$ Cartesian grid centered on the sector where the jet is enforced and with $N_x = N_y = 100$ grid points. All fluxes are averaged in space and time, over 2401 frames once steady state is achieved. Filtered scales s are converted in non-dimensional wavenumber $n = N_x/s$. For both western and eastern jets, fluxes show an upscale energy cascade toward jets' scale and a small range of a downscale cascade at the largest scales for the western jets only.

1.4 Spectral analysis in spherical geometry

Kinetic energy spectra

To compute the spectral analysis of a 2D velocity fields $\mathbf{u}$ projected on a latitude-longitude coordinate grid it is appropriate to decompose the vector field in terms of two scalar functions. A decomposition into rotational (non-divergent) $\mathbf{v}$ and divergent (irrotational) $\mathbf{w}$ velocity components can be performed via the Helmholtz expression $\mathbf{u} = \nabla_h \times \psi \mathbf{e_z} + \nabla_h \phi = \mathbf{v} + \mathbf{w}$, where scalar fields ψ and ϕ are the horizontal (i.e. latitude-longitude) streamfunction and velocity potential, respectively. Using this decomposition, one obtains the vorticity ζ and the divergence δ fields,

$$\zeta = rot_h(\mathbf{u}) = \nabla_h^2 \psi \tag{7a}$$

$$\delta = div_h(\mathbf{u}) = \nabla_h^2 \phi. \tag{7b}$$

By definition, the scalar product of two horizontal vector fields $\mathbf{a}$ and $\mathbf{b}$ can be expressed in the spectral domain as,

$$(\mathbf{a}, \mathbf{b})_{m,n} = \frac{R^2}{n(n+1)} \mathbb{R}\left\{ rot_h(\mathbf{a})_{m,n} rot_h^*(\mathbf{b})_{m,n} + div_h(\mathbf{a})_{m,n} div_h^*(\mathbf{a})_{m,n} \right\} \tag{8}$$

where $*$ is the complex conjugate, $\mathbb{R}\{\cdot\}$ refers to the real part and R is the spherical radius (see Boer (1983); Augier and Lindborg (2013)). It is clear from Eq. (8) that the 2D kinetic energy spectrum (i.e. spectral energy density per modes m, n) is

$$\mathscr{E}(n, m) = \frac{(\mathbf{u}, \mathbf{u})_{m,n}}{2} = \frac{R^2}{2n(n+1)} \mathbb{R}\left\{ \zeta_{m,n} \zeta_{m,n}^* + \delta_{m,n} \delta_{m,n}^* \right\}, \tag{9}$$

where $\zeta_{m,n}$ and $\delta_{m,n}$ are the spherical harmonic coefficients of the relative vorticity and divergence fields. When spherical harmonic functions are invoked to compute energy spectra, the basis functions $Y_n^m(\varphi, \lambda)$ are eigenfunctions of the horizontal Laplacian operator $\nabla_h^2 Y_n^m = -n(n+1) Y_n^m / a^2$, and depend on non-dimensional total and zonal indices n and m respectively (Boer, 1983; Boer and Shepherd, 1983). The planetary spin axis defines the zonal index

$m = 0$ to be the axisymmetric mode that characterizes the zonal jets. Indices $m \neq 0$ define the non-axisymmetric part of the flow, namely velocity fluctuations. Following Sukoriansky et al. (2002), we define the 1D energy spectrum as $E(n) = \sum_{m=-n}^{n} \mathscr{E}(n,m)$, which can be decomposed into a sum of the zonal and Kolmogorov-Kraichnan spectra, $E(n) = E_Z(n) + E_{KK}(n)$. The zonal spectrum corresponds to the axisymmetric energy, $E_Z(n) = \mathscr{E}(n, m = 0)$ while the KK spectrum is a sum over all non-axisymmetric modes, $E_{KK}(n) = 2\sum_{m=1}^{n} \mathscr{E}(n,m)$. In spherical geometry, when the flow approaches the regime of zonostrophic turbulence, the spectra are expected to become,

$$E_Z(n) = C_Z \beta^2 n^{-5}, \tag{10a}$$

$$E_R(n) = C_K \Pi_\epsilon^{2/3} n^{-5/3}, \quad . \tag{10b}$$

One can estimate the scale at which the zonal and KK spectra intersect,

$$L_\beta = 2\pi R (C_K/C_z)^{3/10} (\Pi_\epsilon/\beta^3)^{1/5}. \tag{11}$$

Values for L_β from 2D velocity maps of Cassini and the Saturn GCM are reported in the Table of the letter.

Kinetic energy flux

To compute the non-linear energy flux in the spherical coordinates of Jupiter and Saturn, we start with the vorticity equation,

$$\frac{\partial \zeta}{dt} = -(\mathbf{v} \cdot \nabla)\zeta - D, \tag{12}$$

where $\mathbf{v}$ is the rotational velocity, and D is the vorticity tendency due to divergent flow and other vorticity sources and sinks. In spectral space, the enstrophy equation is

$$\frac{\partial G_n}{dt} = J_n + D_n^G, \tag{13}$$

with enstrophy $G = \frac{1}{2}\zeta^2$, and divergent effects, sources, and sinks contained within D_n^G. The enstrophy interaction term is given by the enstrophy transfer function (Burgess et al., 2013; Read et al., 2018),

$$J_n = -\frac{1}{4} \sum_{m=-n}^{n} \left[\zeta^*_{m,n} \{\mathbf{v} \cdot \nabla\zeta\}_{m,n} + \zeta_{m,n} \{\mathbf{v} \cdot \nabla\zeta\}^*_{m,n} \right], \tag{14}$$

and the associated energy transfer function is

$$I_n = \frac{R^2}{n(n+1)} J_n. \tag{15}$$

The energy flux can now be computed:

$$\Pi_\epsilon^{n+1} = -\sum_{l=1}^{n} I_l \tag{16}$$

respectively. The integral over all wavenumbers N is zero by construction and should also be equal to zero at $n = 0$ as the energy transfer functions represent conservative processes. The expression (16) is an estimate of non-linear transfer of energy between different scales of motions obtained from the spectral decomposition of 2D velocity fields. Energy fluxes for Jupiter and the Saturn GCM are reported in Figure 1 of the main text.

1.5 Potential vorticity formulation and the sorting algorithm

When 2D relative vorticity maps are involved, i.e. from laboratory measurements, global climate models, and Cassini cloud tracking, we estimate the potential vorticity using the formulation

$$PV = (\zeta + 2\Omega)/H, \tag{17}$$

where H is the fluid layer depth. In the laboratory it corresponds to the topography of the free surface H, while for the Saturn GCM and for Jupiter we consider a constant depth extension of the atmospheric layer along the planetary radius, using $H = 59$ km in the Saturn GCM (Spiga et al., 2020) and $H = 1000$ km for Jupiter (Kaspi et al., 2018).

For Jupiter and Saturn, we also make use of potential vorticity profiles derived by Read et al. (2006) for Jupiter and by Read et al. (2009) for Saturn. These are isentropic potential vorticity (IPV) profiles computed from measured horizontal velocity and temperature fields, assuming hydrostatic balance and large Richardson number (i.e. when buoyancy forces dominate over velocity shear in the vertical). Then the general definition of Ertel PV becomes

$$IPV = -g(\zeta_p + 2\Omega \sin\theta)\frac{\partial \Theta}{\partial p} \tag{18}$$

where ζ_p is the vertical component of the relative vorticity on pressure surfaces, g is the gravitational constant, Θ is the potential temperature, and p is the pressure. The quasi-geostrophic potential vorticity (QGPV) is defined on isobaric surfaces,

$$QGPV = \zeta_p + 2\Omega \sin\theta - f\left[\frac{\partial}{\partial p}\left(\frac{pT_d(x,y,p)}{s(p)T_s(p)}\right)\right], \tag{19}$$

where $T_s(p)$ is the horizontal mean temperature profile, representing the reference profile for the quasi-geostrophic analysis, $T_d(x,y,p) = T(x,y,p) - T_s(p)$, and $s(p)$ is the profile of the stability parameter, defined in terms of potential temperature as $s = -pC_{p0}/\langle C_p(p)\rangle \partial\langle ln\Theta\rangle/\partial lnp$. Here horizontal means isobaric surface and defines the coordinates (x, y), C_p is the specific heat capacity of hydrogen, and C_{p0} is the specific heat capacity of the hydrogen-helium mixture that dominates the composition of gas giants' atmospheres (see Read et al. (2006, 2009) for more details).

Potential vorticity monotonization is performed by using the Matlab function "sort" that sorts array elements in either the ascending or descending direction. Each PV value in the array is located at a certain index corresponding to a spatial position in a radial or latitudinal array. The radial and latitudinal arrays are regular grids with spacing Δ_g. Once sorted, each PV value has moved from its indexed position to another, and the displacement in the indexed array is converted into a length scale by multiplying by the grid spacing Δ_g. Finally, the typical length scale L_M is obtained by computing the RMS displacement over time and space, excluding zeros. The algorithm of the sorting procedure is available at `https://github.com/scabanes/JUMP`

1.6 Estimate of L_M and L_β in the main manuscript Table

For the laboratory: Estimates of L_M and L_β are computed on truncated (i.e. 90° or 180° azimuthal domains) surface velocity maps with maximum cylindrical radius $R = 0.297$ m. Spectral quantities are averaged over 2401 frames corresponding to 58 rotation periods. Length scales L_M are RMS values with their standard deviation over the same truncated domain and the same 2401 frames.

For Jupiter: Estimates of L_M based on QGPV (CIRS) and QGPV (IRIS) are computed between the range of latitudes ±58° and ±10°. Estimates are RMS values in latitude and over four pressure levels between $2 \leq p \leq 268$ hPa (for CIRS) and $2 \leq p \leq 225$ hPa (for IRIS) respectively (profiles are shown in supplementary Fig. 5 and 6). Estimates of L_M and L_β from

the 2D Cassini maps are computed between latitudes ±55° at Jupiter's cloud deck, i.e. approximatively $550 \leq p \leq 750$ hPa (Porco et al., 2003). Spectral quantities are averaged over four Jupiter days and the length scale L_M is an RMS value with its standard deviation over latitude, longitude and time.

For Saturn: Estimates of L_M from QGPV and IPV are computed between the range of latitudes ±58° and ±10°. Estimates are RMS values in latitude and over four pressure levels between $2 \leq p \leq 270$ hPa (profiles are shown in supplementary Fig. 8 and 9). Estimates of L_M and L_β from the Saturn GCM are computed between latitudes ±80°. Spectral quantities are averaged over two simulated Saturn years and over nine pressure levels ranging between $30 < p < 650$ hPa. The length scale L_M is an RMS value with its standard deviation over latitude, longitude, pressure, and the two simulated Saturn years.

Here, our procedure to estimate L_M and L_β is based on a global average over time, latitudes, longitudes and pressure levels and presupposes the existence of a global value for the energy transfer rate Π_ϵ. Further studies might consider a more local (at smaller scale) estimate of the turbulent energy transfers Π_ϵ rather than global, but this is beyond the scope of this study.

1.7 Eddy diffusivity coefficient in quasi-geostrophic turbulence

In theories of homogeneous isotropic turbulence, it is customary to invoke a one-dimensional representation of the eddy diffusivity coefficient K which is given by the classical Richardson diffusion law (Richardson, 1926),

$$K(l) \propto \Pi_\epsilon^{1/3} l^{4/3}, \tag{20}$$

where Π_ϵ is the rate of a direct energy cascade and l a typical mixing length scale. However, geophysical and planetary turbulence features strongly anisotropic flows that combine turbulence, waves and jets. Energy is transfered upscale by an inverse energy cascade and the effect of the anisotropy is reflected in the choice of l in the meridional direction (along the latitude).

In the framework of rotating turbulence with a β-effect, recall the critical length scale L_β that corresponds to the crossover between the KK-spectrum and the zonal flow spectrum, see expressions (2) and (3) in the main manuscript. In the meridional direction, scales l larger than L_β do not contribute to the diffusivity coefficient $K(l)$ and so l in (20) remains "frozen" at L_β and becomes scale-independent, something reminiscent of the so-called Taylor diffusion regime (Taylor, 1922). Then, following the formulation developed by Galperin et al. (2016), one can obtain the expression for the latitudinal eddy diffusivity coefficient in the scale-independent, Taylor-like regime,

$$K_\theta(L_\beta) = \Pi_\varepsilon^{3/5} \beta^{-4/5}, \tag{21}$$

where Π_ε is the upscale energy transfer rate discussed in the main text. This scaling was verified in laboratory experiments and gave great prediction of the meridional spread of comet's debris in planetary atmospheres using a one-dimensional diffusion equation, see Galperin et al. (2016). Note that in the zonal direction, diffusion continue to obey the Richardson law in expression (20). We estimate K_θ within Jupiter's atmosphere using $\beta \simeq 2.5 \times 10^{-12}$ m^{-1} s^{-1}, $1.5 \times 10^{-5} \leq \Pi_\epsilon \leq 9 \times 10^{-5}$ and within Saturn's atmosphere using $\beta \simeq 2.83 \times 10^{-12}$ m^{-1} s^{-1}, $0.6 \times 10^{-5} \leq \Pi_\epsilon \leq 1.2 \times 10^{-5}$ respectively. This results in $K_\theta \sim (2.4 - 7) \times 10^6$ m^2 s^{-1} for Jupiter and $\sim (1.3 - 1.9) \times 10^6$ m^2 s^{-1} for Saturn.

2 Supplementary Tables and Figures

References

Arfken, G. B. and Weber, H. J. (1999). Mathematical Methods for Physicists.

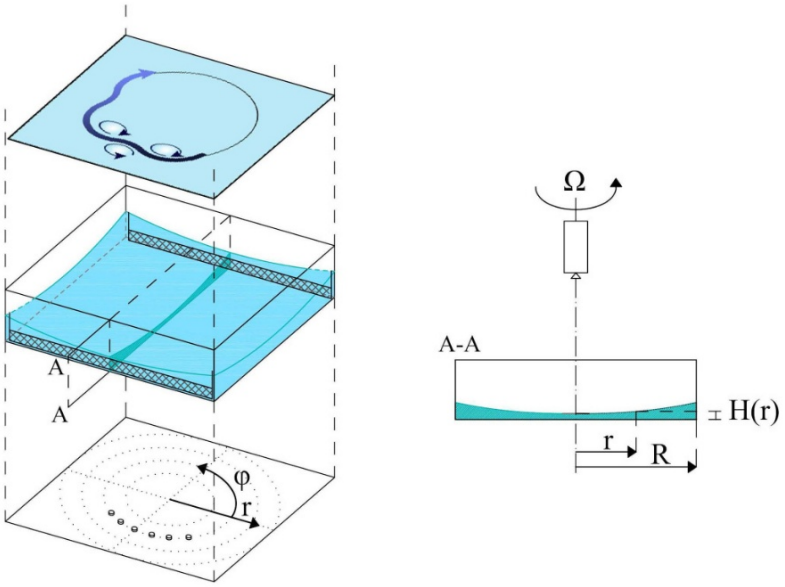

Figure 1: Schematic representation of the experimental device. magnets are placed in a 90° arc at radius 17 cm. The topographic β-effect is estimated by $\beta = (2\Omega/H)dH/dr$ and depends on the fluid column height H and the cylindrical radius r.

Augier, P. and Lindborg, E. (2013). A new formulation of the spectral energy budget of the atmosphere, with application to two high-resolution general circulation models. *Journal of the Atmospheric Sciences*, 70(7):2293–2308.

Boer, G. J. (1983). Homogeneous and isotropic turbulence on the sphere. *Journal of the Atmospheric Sciences*, 40(1):154–163.

Boer, G. J. and Shepherd, T. (1983). Large-scale two-dimensional turbulence in the atmosphere. *Journal of the Atmospheric Sciences*, 40(1):164–184.

Boffetta, G. and Musacchio, S. (2010). Evidence for the double cascade scenario in two-dimensional turbulence. *Physical Review E*, 82(1):016307.

Burgess, B. H., Erler, A. R., and Shepherd, T. G. (2013). The troposphere-to-stratosphere transition in kinetic energy spectra and nonlinear spectral fluxes as seen in ecmwf analyses. *Journal of the Atmospheric Sciences*, 70(2):669–687.

Chen, S., Ecke, R. E., Eyink, G. L., Rivera, M., Wan, M., and Xiao, Z. (2006). Physical mechanism of the two-dimensional inverse energy cascade. *Physical review letters*, 96(8):084502.

Conrath, B. J., Gierasch, P. J., and Ustinov, E. A. (1998). Thermal Structure and Para Hydrogen Fraction on the Outer Planets from Voyager IRIS Measurements. *Icarus*, 135(2):501–517.

Espa, S., Lacorata, G., and Di Nitto, G. (2014). Anisotropic Lagrangian dispersion in rotating flows with a β effect. *Journal of Physical Oceanography*, 44(2):632–643.

Galperin, B., Hoemann, J., Espa, S., and Di Nitto, G. (2014a). Anisotropic turbulence and Rossby waves in an easterly jet: An experimental study. *Geophysical Research Letters*, 41(17):6237–6243.

Galperin, B., Hoemann, J., Espa, S., Di Nitto, G., and Lacorata, G. (2016). Anisotropic macroturbulence and diffusion associated with a westward zonal jet: From laboratory to planetary atmospheres and oceans. *Physical Review E*, 94(6):063102.

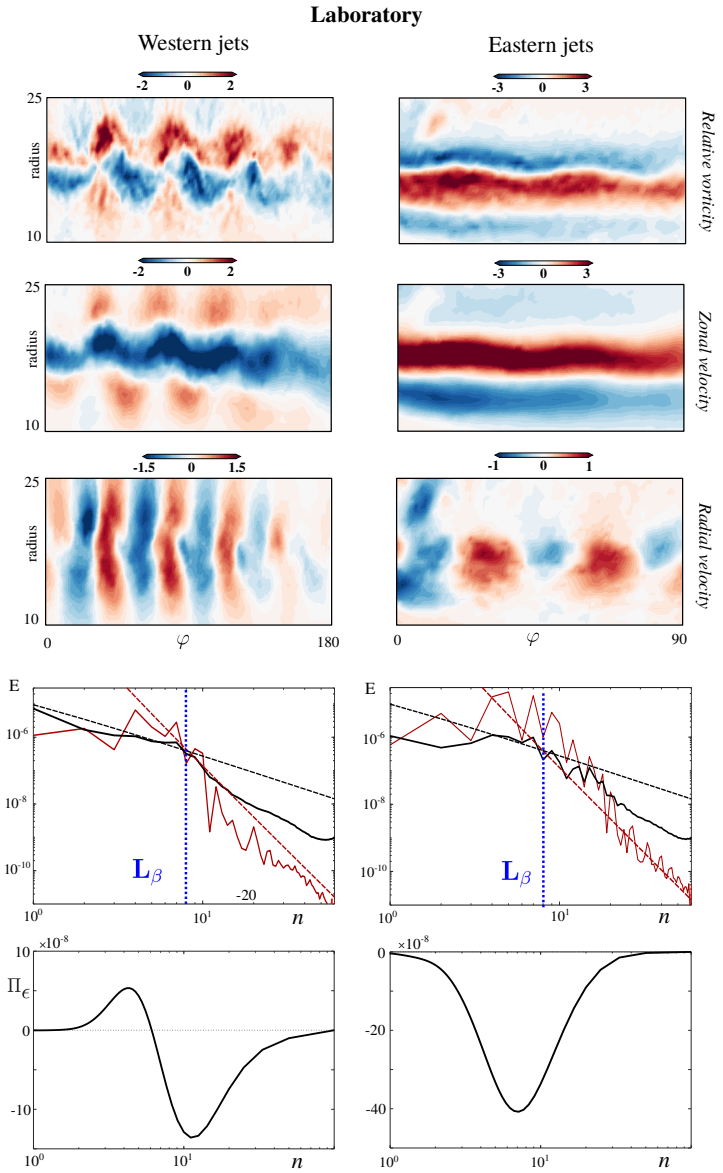

Figure 2: Laboratory fields and spectral analysis. From top to bottom, vorticity (s^{-1}), zonal velocity (m s^{-1}) and radial velocity (m s^{-1}) fields as well as the spectral distribution of kinetic energy (m^2 s^{-2}). All quantities are reported for an western (eastern) jet forced by a 180° (90°) arc of magnets with a forcing that corresponds to an electrical current of $I = 6$A. Energy spectra and fluxes are computed from instantaneous velocity maps at steady state and averaged in time at each mode n over 58 rotation periods.

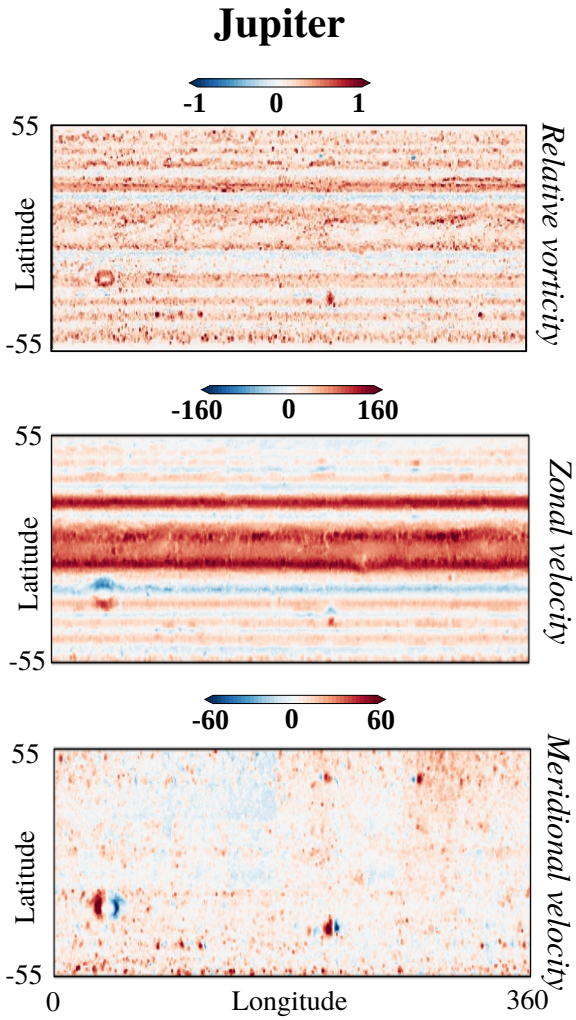

Figure 3: Jupiter's cloud-top winds based on Cassini imaging. 2D horizontal velocity maps were obtained by Galperin et al. (2014b) using cloud tracking of high resolution visible/NIR images taken during Cassini's flyby of Jupiter in December 2000. Wind fields were retrieved by using Correlation Imaging Velocimetry. We used their dataset G14g, which contains gridded horizontal wind vectors covering three rotation periods over 360° in longitude and ±50° in latitude. Here the second day is shown. Top to bottom: Relative vorticity is in units of $\times 10^{-4}$ s^{-1}, zonal velocity in m s^{-1}, and meridional velocity in m s^{-1}.

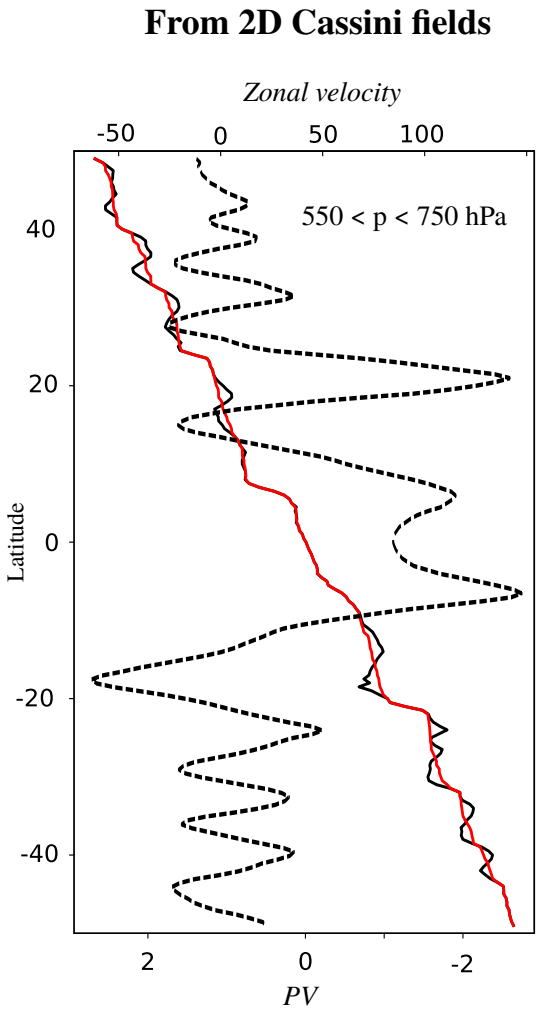

Figure 4: Jupiter potential vorticity and averaged zonal velocity profiles. PV is shown in thick black lines in units of $\times 10^{-4}$ s^{-1}. Zonal velocity are dashed lines in units of m s^{-1}. Red lines are monotonized PV profiles. The pressure level p at which profiles are measured in the atmosphere are labeled in the panel.

Table 1: Control parameters used in laboratory experiments with electromagnetic forcing inducing westward and eastward momentum with an electrical current intensity I in ampere (A). Westward jets are produced with a 90° and a 180° arc of magnets while eastward jets are produced using a 90° arc of magnets only. Π_ϵ is the energy transfer rate, $\hat{L}_\beta$ is the transitional scale in cylindrical geometry, and n is the index at which the spectra intersect. L_β in the main manuscript Table corresponds to $\hat{L}_\beta$ here.

Experiments	I (A)	Π_ϵ (W kg^{-1})	$\hat{L}_\beta$ (cm)	n
1: Western-jet 90°	2	$2.1 \cdot 10^{-8}$	2.2	12
2: Western-jet 90°	4	$11 \cdot 10^{-8}$	3.1	9
3: Western-jet 90°	6	$29 \cdot 10^{-8}$	3.72	8
1: Eastern-jet 90°	2	$2.1 \cdot 10^{-8}$	2.2	12
2: Eastern-jet 90°	4	$11 \cdot 10^{-8}$	3.1	9
3: Eastern-jet 90°	6	$21 \cdot 10^{-8}$	3.5	8
1: Western-jet 180°	2	$2 \cdot 10^{-8}$	2.24	14
2: Western-jet 180°	4	$8 \cdot 10^{-8}$	2.91	10
3: Western-jet 180°	6	$20 \cdot 10^{-8}$	3.46	8

Galperin, B., Sukoriansky, S., and Dikovskaya, N. (2010). Geophysical flows with anisotropic turbulence and dispersive waves: flows with a β-effect. *Ocean Dynamics*, 60(2):427–441.

Galperin, B., Young, R. M. B., Sukoriansky, S., Dikovskaya, N., Read, P. L., Lancaster, A. J., and Armstrong, D. (2014b). Cassini observations reveal a regime of zonostrophic macroturbulence on Jupiter. *Icarus*, 229:295–320.

Kaspi, Y., Galanti, E., Hubbard, W. B., Stevenson, D. J., Bolton, S. J., Iess, L., Guillot, T., Bloxham, J., Connerney, J. E. P., Cao, H., et al. (2018). Jupiter's atmospheric jet streams extend thousands of kilometres deep. *Nature*, 555(7695):223–226.

Lacorata, G. and Espa, S. (2012). On the influence of a β-effect on lagrangian diffusion. *Geophysical Research Letters*, 39(11):L11605.

Porco, C. C., West, R. A., McEwen, A., Del Genio, A. D., Ingersoll, A. P., Thomas, P., Squyres, S., Dones, L., Murray, C. D., Johnson, T. V., et al. (2003). Cassini imaging of Jupiter's atmosphere, satellites, and rings. *Science*, 299(5612):1541–1547.

Porco, C. C., West, R. A., Squyres, S., McEwen, A., Thomas, P., Murray, C. D., Del Genio, A., Ingersoll, A. P., Johnson, T. V., Neukum, G., et al. (2004). Cassini imaging science: Instrument characteristics and anticipated scientific investigations at Saturn. *Space Science Reviews*, 115:363–497.

Read, P. L., Conrath, B. J., Fletcher, L. N., Gierasch, P. J., Simon-Miller, A. A., and Zuchowski, L. C. (2009). Mapping potential vorticity dynamics on Saturn: Zonal mean circulation from Cassini and Voyager data. *Planetary and Space Science*, 57(14-15):1682–1698.

Read, P. L., Gierasch, P. J., Conrath, B. J., Simon-Miller, A., Fouchet, T., and Yamazaki, Y. H. (2006). Mapping potential-vorticity dynamics on Jupiter. I: Zonal-mean circulation from Cassini and Voyager 1 data. *Quarterly Journal of the Royal Meteorological Society*, 132(618):1577–1603.

Read, P. L., Tabataba-Vakili, F., Wang, Y., Augier, P., Lindborg, E., Valeanu, A., and Young, R. M. B. (2018). Comparative terrestrial atmospheric circulation regimes in simplified global circulation models. Part II: Energy budgets and spectral transfers. *Quarterly Journal of the Royal Meteorological Society*, 144(717):2558–2576.

Richardson, L. F. (1926). Atmospheric diffusion shown on a distance-neighbour graph. *Proceedings of the Royal Society of London. Series A, Containing Papers of a Mathematical and Physical Character*, 110(756):709–737.

Spiga, A., Guerlet, S., Millour, E., Indurain, M., Meurdesoif, Y., Cabanes, S., Dubos, T., Leconte, J., Boissinot, A., Lebonnois, S., Sylvestre, M., and Fouchet, T. (2020). Global climate modeling of Saturn's atmosphere. Part II: Multi-annual high-resolution dynamical simulations. *Icarus*, 335:113377.

Sukoriansky, S., Galperin, B., and Dikovskaya, N. (2002). Universal spectrum of two-dimensional turbulence on a rotating sphere and some basic features of atmospheric circulation on giant planets. *Physical Review Letters*, 89(12):124501.

Taylor, G. I. (1922). Diffusion by continuous movements. *Proceedings of the london mathematical society*, 2(1):196–212.

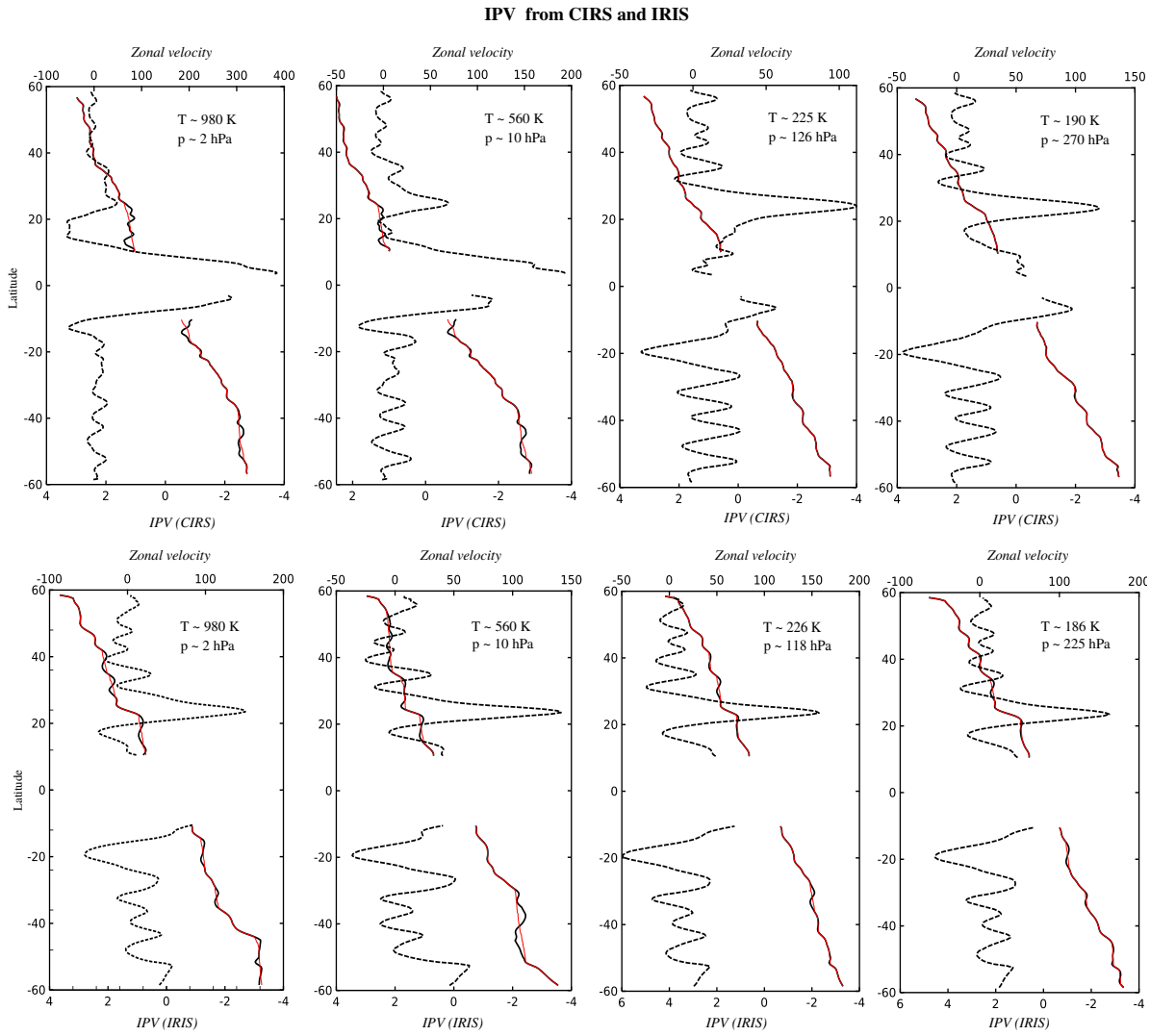

Figure 5: Jupiter IPV and averaged zonal velocity profiles. To compute IPV latitudinal profiles for Jupiter (limited to the range of latitudes ±58° and ±10°), Read et al. (2006) combined velocity measurements, derived by tracking cloud features in Voyager 1 and 2 and Cassini images, and thermal measurements from the Voyager 1 InfraRed Interferometric Spectrometer (IRIS) (Conrath et al., 1998) and Cassini Composite InfraRed Spectrometer (CIRS) (Porco et al., 2004) instruments. IPV from CIRS and IRIS instruments are shown as black thick lines in units of $\times 10^{-4}$ s^{-1}, and zonal velocity is shown as dashed lines in units of m s^{-1}. The red lines are monotonized IPV profiles. The pressure level p and the temperature T of the isentropic level at which profiles are measured in the atmosphere, are labeled in each panel. For more details on IPV profiles see Read et al. (2006).

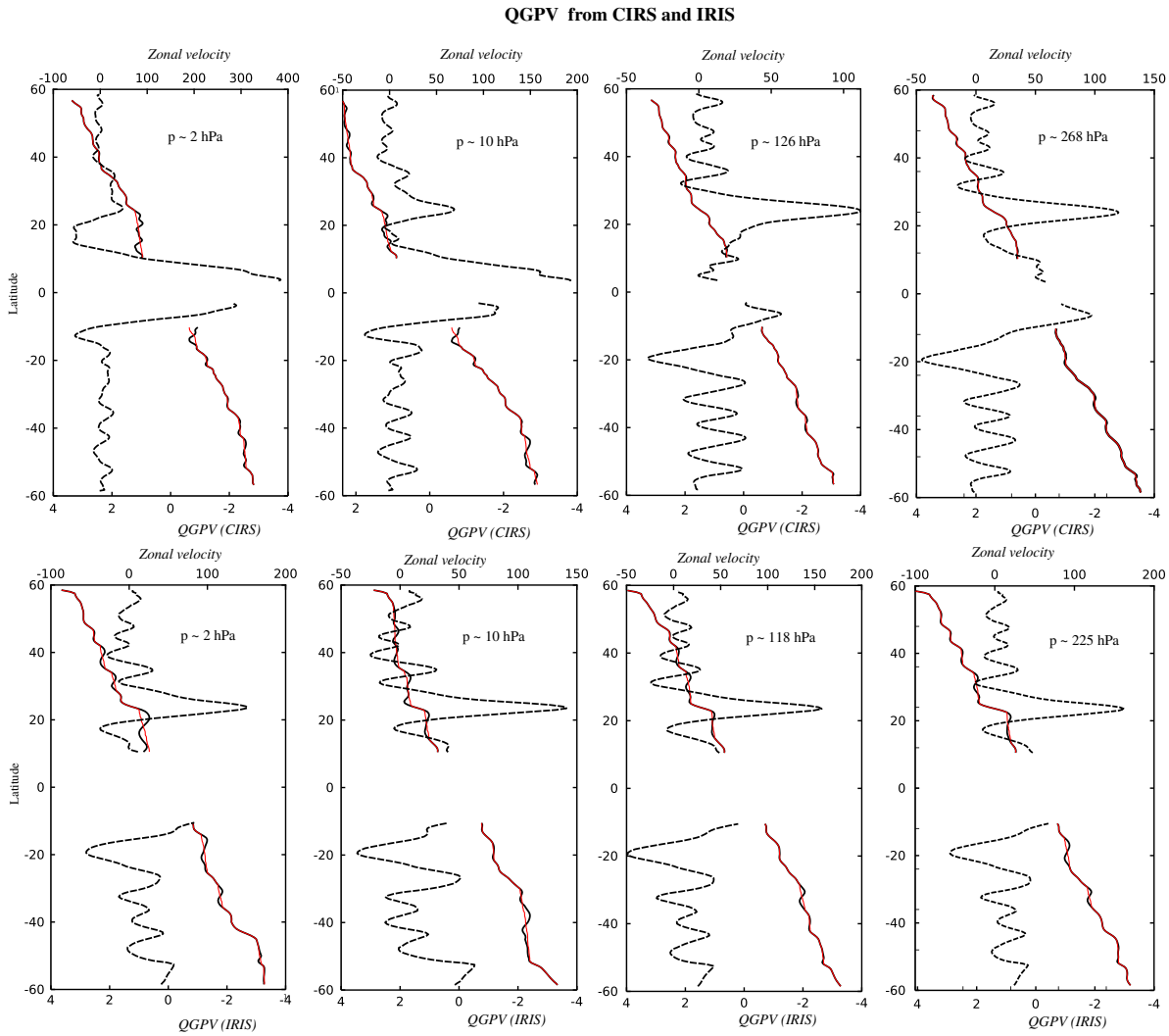

Figure 6: Jupiter QGPV and averaged zonal velocity profiles. To compute QGPV latitudinal profiles for Jupiter (limited to the range of latitudes ±58° and ±10°), Read et al. (2006) combined velocity measurements, derived by tracking cloud features in Voyager 1 and 2 and Cassini images, and thermal measurements from the Voyager 1 InfraRed Interferometric Spectrometer (IRIS) (Conrath et al., 1998) and Cassini Composite InfraRed Spectrometer (CIRS) (Porco et al., 2004) instruments. QQPV from CIRS and IRIS instruments are shown as black thick lines in units of $\times 10^{-4}$ s^{-1}, and zonal velocity is shown as dashed lines in units of m s^{-1}. The red lines are monotonized QGPV profiles. The pressure level p where profiles are measured are labeled in each panel. For more details on QGPV profiles see Read et al. (2006).

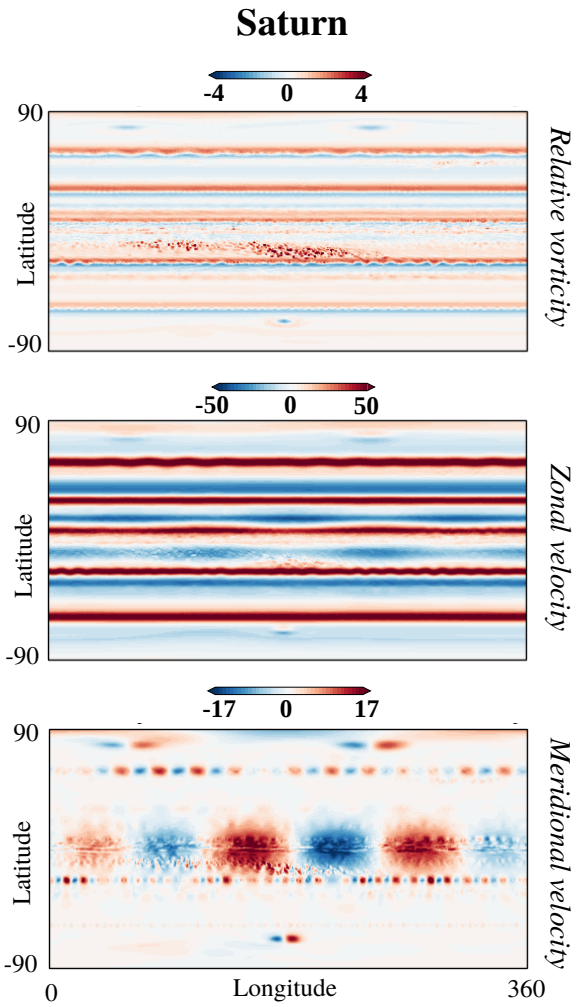

Figure 7: Saturn GCM fields. From top to bottom: Relative vorticity in units of $\times 10^{-5}$ s^{-1}, zonal velocity in m s^{-1}, and meridional velocities in m s^{-1}.

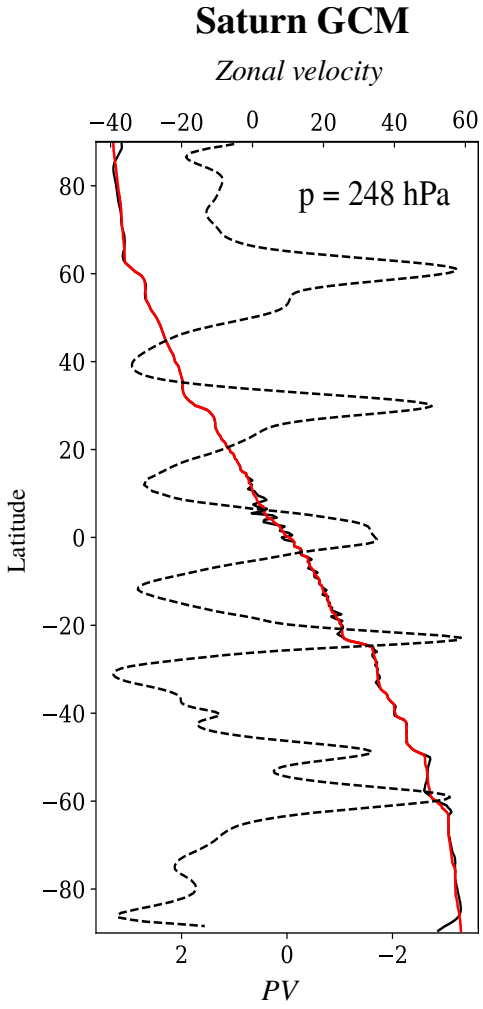

Figure 8: Saturn potential vorticity and averaged zonal velocity profiles. PV is shown in thick black lines in units of $\times 10^{-4}$ s^{-1}. Zonal velocity are dashed lines in units of m s^{-1}. Red lines are monotonized PV profiles. The pressure level p at which profiles are measured in the atmosphere are labeled in the panel.

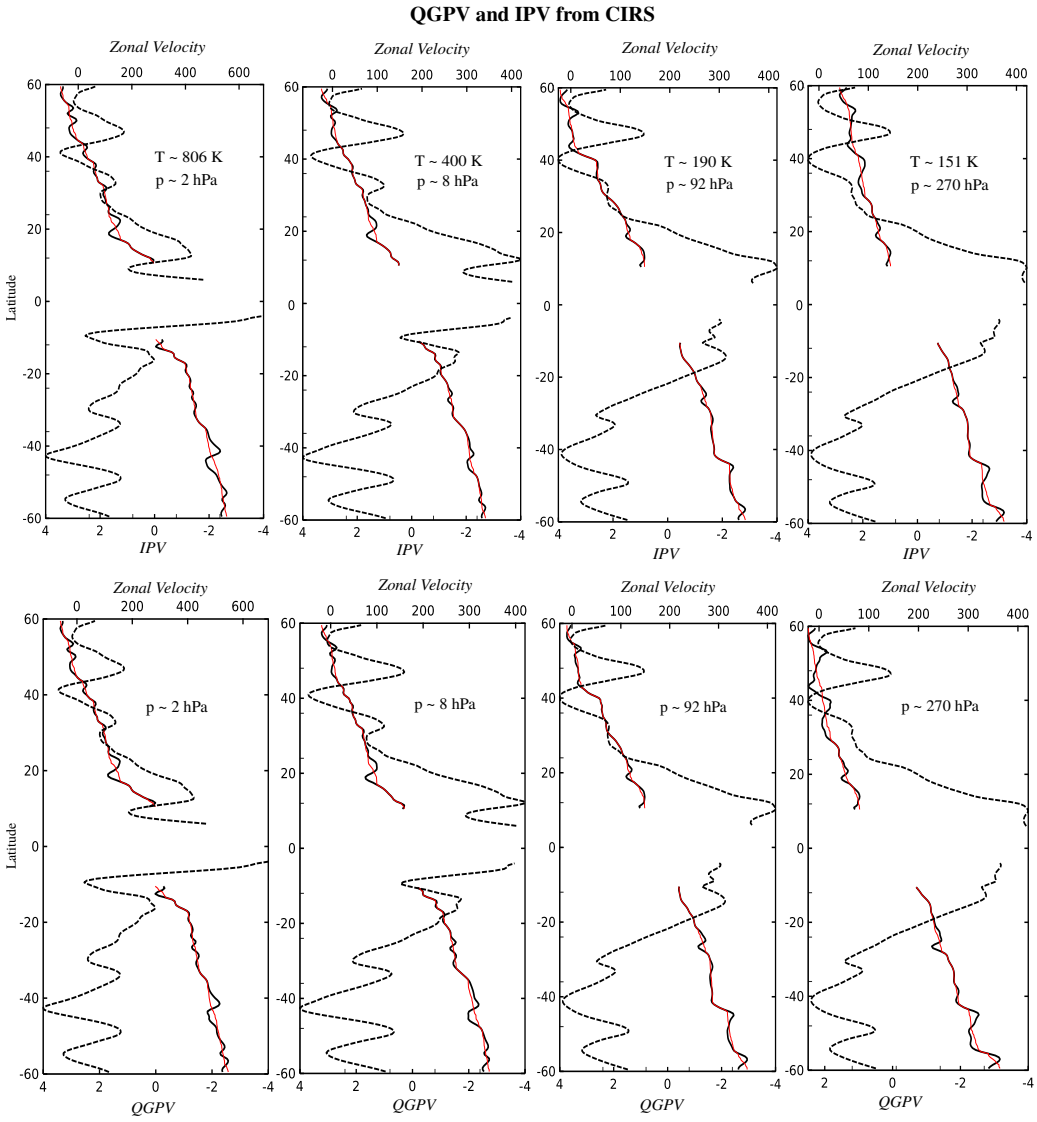

Figure 9: Saturn potential vorticity and averaged zonal velocity profiles. We show IPV and QGPV measured from CIRS-instrument and represented in thick black lines in units of $\times 10^{-4}$ s^{-1}. Zonal velocity are dashed lines in units of m s^{-1}. Red lines are monotonized QGPV and IPV profiles. The temperature of the isentropic level and/or the pressure level p at which profiles are measured in the atmosphere, are labeled in each panel. For more details on the IPV and QGPV profiles see Read et al. (2009).